Journal of Sound and Vibration 330 (2011) 6036–6052

Contents lists available at ScienceDirect

Journal of Sound and Vibration

journal homepage: www.elsevier.com/locate/jsvi

Relative performance of a vibratory energy harvester in mono- and bi-stable potentials

Ravindra Masana, Mohammed F. Daqaq *

Nonlinear Vibrations and Energy Harvesting Lab. (NOVEHL), Department of Mechanical Engineering, Clemson University, Clemson, SC 29634, Unites States

ARTICLE INFO

Article history:
Received 25 October 2010
Received in revised form
21 July 2011
Accepted 22 July 2011
Handling Editor: M.P. Cartmell
Available online 6 August 2011

ABSTRACT

Motivated by the need for broadband vibratory energy harvesting, many research studies have recently proposed energy harvesters with nonlinear characteristics. Based on the shape of their potential function, such devices are classified as either *mono-* or *bi-stable* energy harvesters. This paper aims to investigate the relative performance of these two classes under similar excitations and electric loading conditions. To achieve this goal, an energy harvester consisting of a clamped–clamped piezoelectric beam bi-morph is considered. The shape of the harvester's potential function is altered by applying a static compressive axial load at one end of the beam. This permits operation in the mono-stable (pre-buckling) and bi-stable (post-buckling) configurations. For the purpose of performance comparison, the axial load is used to tune the harvester's oscillation frequencies around the static equilibria such that they have equal values in the mono- and bi-stable configurations. The harvester is subjected to harmonic base excitations of different magnitudes and a slowly varying frequency spanning a wide band around the tuned oscillation frequency. The output voltage measured across a purely resistive load is compared over the frequency range considered. Two cases are discussed; the first compares the performance when the bi-stable harvester has deep potential wells, while the second treats a bi-stable harvester with shallow wells. Both numerical and experimental results demonstrate the essential role that the potential shape plays in conjunction with the base acceleration to determine whether the bi-stable harvester can outperform the mono-stable one and for what range of frequencies. Results also illustrate that, for a bi-stable harvester with shallow potential wells, super-harmonic resonances can activate the inter-well dynamics even for a small base acceleration, thereby producing large voltages in the low frequency range.

1. Introduction

Recent advances in electronics and other fields of technology have led to the fabrication of low cost and low power-consumption sensors [1,2]. Today, many sensing systems, such as those used for health monitoring of structures and machines, can operate efficiently without significant power requirements [3–7]. For instance, a wireless transponder for data transmission can operate efficiently with less than 1 mW of power [1,2]. A sensor interface chip for health monitoring that consists of a sensor and a micro-controller has an average power consumption of 48 μW [4,5].

Unfortunately, effective usage of these sensors is currently being hindered by their power sources, usually batteries that have fixed storage capacity and low energy density [8]. To overcome this issue, many research studies are currently being

* Corresponding author.
E-mail address: mdaqaq@clemson.edu (M.F. Daqaq).

0022-460X/$ - see front matter © 2011 Elsevier Ltd. All rights reserved.
doi:10.1016/j.jsv.2011.07.031

directed toward scavenging otherwise wasted energy from the ambient environment to power these sensors. Various energy harvesters have been developed to transform mechanical motions directly into electricity [6]. This is realized by exploiting the ability of some active materials and electromechanical mechanisms to generate an electric potential in response to mechanical stimuli and external vibrations [9–11].

Traditionally, vibratory energy harvesters have been designed with linear characteristics [12–15]. These linear designs, however, have demonstrated some critical issues that limit their effectiveness. Specifically, since their electromechanical transduction is enhanced only in a small frequency bandwidth where the excitation frequency is very close to the fundamental frequency of the harvester (resonance condition), any variations in the excitation frequency around the harvester's fundamental frequency decreases the coupling between the source and the harvesting device and reduces the output power significantly. This becomes an even more pressing issue when one realizes that most environmental excitations have broadband or time-dependent characteristics in which the energy is distributed over a wide spectrum of frequencies or the dominant frequencies drift with time.

To circumvent this problem, tunable harvesters whose fundamental frequency can be altered actively or passively to match the dominant excitation frequency were developed [14,16–20]. Such tunable designs which usually require external power sources can only account for slow and small drifts in the excitation frequency and are not ideal for excitations having random frequency characteristics [14].

A significant number of research studies are currently focused on the idea of purposefully incorporating nonlinearities into the harvester's design so as to extend its bandwidth and enhance its performance in a non-stationary vibratory environment [19,21–26]. One class of nonlinear harvesters incorporates cubic stiffness nonlinearities. The potential energy function of these harvesters exhibits *mono-stable* characteristics that can enhance the frequency bandwidth under steady-state fixed-frequency harmonic excitations. Stanton et al. [27] have demonstrated that the bend in the frequency–response curves resulting from the nonlinearity can be beneficial when harvesting energy from excitation sources having a time-varying frequency. However, Daqaq [28] and Barton et al. [29] have recently shown that the nonlinearity in mono-stable harvesters has an adverse influence on the mean output power under colored random excitations [28,29].

A new class of nonlinear harvesters with a *bi-stable* potential has been recently investigated as a possible solution to improve the performance of energy harvesters in non-stationary vibratory environments [23–26,30]. As shown in Fig. 1, an energy harvester with a bistable potential has two stable equilibria separated by a potential barrier (an unstable saddle). When sufficient energy is supplied to the system, dynamic trajectories overcome the potential barrier and escape from one potential well to the other activating the inter-well dynamics. This non-resonant behavior permits coupling between the environmental excitation and the energy harvester over a wider range of frequencies. It has been shown that when, carefully designed, bi-stable harvesters can provide significant power levels over a wide range of frequencies under steady-state harmonic excitations [25,26].

McInnes et al. [30] have also investigated the utilization of a bi-stable harvester in conjunction with the stochastic resonance phenomenon to enhance the transduction of vibratory energy harvesters. For the purpose of evaluation, they proposed a conceptual model of a bi-stable device consisting of an axially loaded buckled clamped–clamped beam, similar to the one considered in this paper. They demonstrated that enhanced transduction is realized by superimposing a periodic forcing on a white noise Gaussian input. Such findings are of significant importance for energy harvesting because many environmental excitations consist of a combination of periodic and random inputs.

As of today, there are no studies addressing the relative performance of nonlinear energy harvesters, especially those of different potential characteristics. A few research publications have already illustrated that bi-stable harvesters can provide large amplitude voltages over a wide range of frequencies but these results have never been compared to the mono-stable results for the same range of frequencies and similar levels of input accelerations. Such studies are essential to shed more light onto the relative performance characteristics of bi-stable harvesters as compared to the mono-stable designs. To that end, we consider a clamped–clamped axially loaded piezoelectric beam bi-morph which can operate as an energy harvester in the mono-stable (pre-buckling) and bi-stable (post-buckling) configurations [20,30,31]. For the purpose of comparison, a compressive static axial load is used to tune the harvester's oscillation frequencies around the

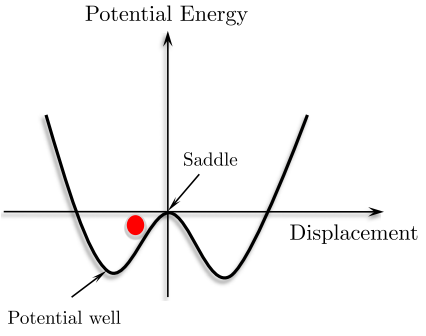

Fig. 1. Shape of the potential energy function for a bi-stable harvester.

stable static equilibria such that they have equal values in the mono- and bi-stable configurations. The harvester is then subjected to harmonic base excitations of different magnitudes and a slowly varying frequency spanning a wide band around the tuned oscillation frequency. The output voltage is measured and compared over the frequency range considered. Both theoretical and experimental findings are used to delineate the important role that the magnitude of base acceleration plays in conjunction with the potential shape of the harvester to characterize the comparative performance and behavior in both configurations.

2. Axially loaded nonlinear energy harvester

To achieve the objectives of this work, we consider the tunable axially loaded energy harvester shown in Fig. 2. The harvester, which has been modeled extensively in one of our previous publications [19], consists of a thin metal beam of length, L, thickness, t_s, width b_s, and Young's modulus, C_s. The beam is clamped on both sides and sandwiched between two piezoelectric patches of length L_2-L_1, thickness t_p, width b_p, and Young's modulus, C_p. The beam is subjected to a compressive static axial loading, P, and a transverse dynamic excitation, $a_b(t)$. The axial load is used in this study to control the beam's fundamental frequency in both the mono- and bi-stable configurations by softening and hardening the structure, respectively. In response to the dynamic excitation, the beam undergoes finite amplitude oscillations about a static position defined by the axial load, P. These oscillations produce a dynamic strain in the piezoelectric patches which, in turn, produce a voltage difference across a purely resistive load, R.

2.1. Experimental setup

To carry the experimental component of this work, the setup shown in Fig. 3 is used. The system consists of a clamped–clamped aluminum beam with two piezoelectric patches attached to either surface of the beam using a conductive silver epoxy resin. The patches which have a series connection are also connected in parallel to a purely resistive electric load. The boundary conditions were created using aluminum clamps carefully designed to minimize slipping at either end of the beam. One of the clamps is placed on a linear sliding bearing to facilitate the exertion of an axial load for the purpose of frequency tuning. The axial force is exerted using a bolt with a locking nut to keep it in place, and the force is measured using a force sensor. The geometric and material properties of the structure are listed in Table 1.

2.2. Mono- versus bi-stable configurations

The axially loaded harvester considered can operate in the mono- and bi-stable configurations by simply altering the applied axial load. When the axial load is below the critical buckling load, the beam exhibits one stable equilibrium position and beam oscillations are confined to one global potential well (*mono-stable configuration*). On the other hand, when the axial load is larger than the critical buckling load, the beam has two locally stable equilibria separated by an unstable saddle (*bi-stable configuration*). To model the global behavior of the beam in both configurations, we adopt the reduced-order single-mode electromechanical model we have recently developed and experimentally validated in [19]. The reader can refer to Appendix A for details. Under the assumption that the mid-span static deflection of the beam is small in the bi-stable case and that the excitation frequency is always close to the frequency of the first mode which is

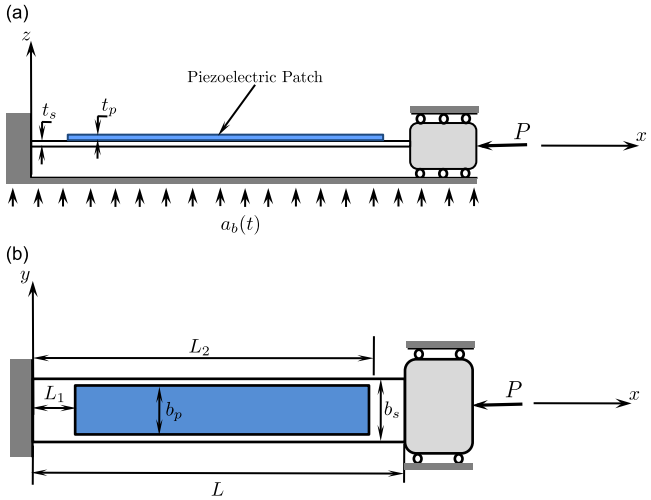

Fig. 2. Schematic of an axially loaded energy harvester. Here, L is the length of the metal beam, t_s is its thickness, and b_s is its width. The distance L_2-L_1 denotes the length of the piezoelectric patch, t_p denotes its thickness, and b_p denotes its width. The beam is subjected to a compressive static axial loading, P, and a transverse dynamic excitation, $a_b(t)$.

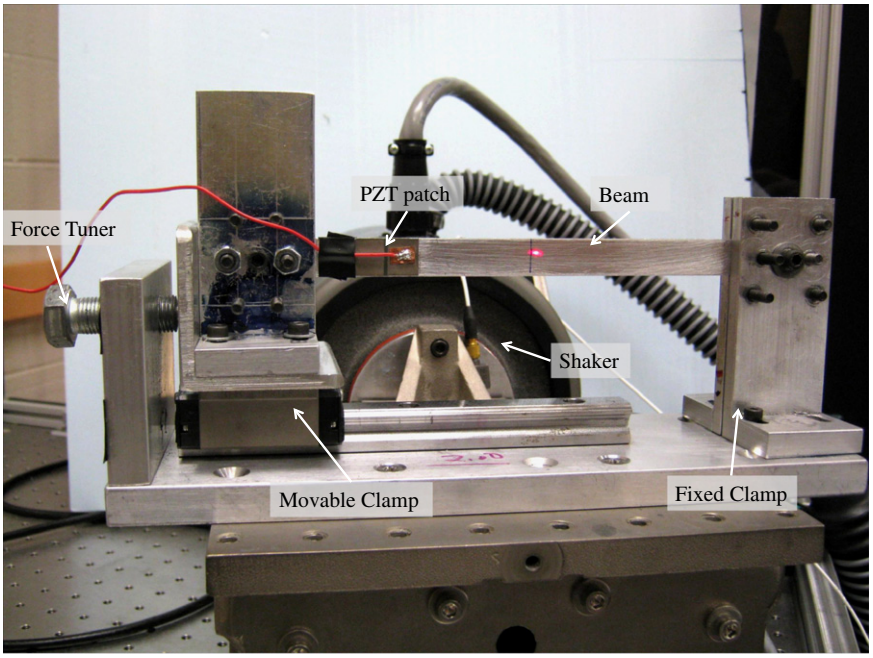

Fig. 3. Setup of the harvester used in the experiments.

Table 1
Material and geometric properties of the harvester.

Parameter (symbol)	**Value**
Structural member	
Young's modulus (C_s)	69 GPa
Mass density (ρ_s)	2700 kg m^{-3}
Length (L)	15.00×10^{-2} m
Width (b_s)	1.32×10^{-2} m
Thickness (t_s)	6.35×10^{-4} m
Piezoelectric member	
Young's modulus (C_p)	62 GPa
Mass density (ρ_p)	7800 kg m^{-3}
Length (L_1)	1.27×10^{-2} m
Length (L_2)	3.43×10^{-2} m
Width (b_p)	1.27×10^{-2} m
Thickness (t_p)	1.90×10^{-4} m
Permittivity (ε)	3800
Piezoelectric constant (e_{31})	-19.84 C m^{-2}

assumed to be free of any internal resonances or an external combination resonance with any of the other modes, we can write

$$m\ddot{q}+c\dot{q}+k(1-\alpha P)q+\lambda(1-\beta P)q^3+\theta V=-mf_1a_b(t), \tag{1a}$$

$$-\theta\dot{q}+C_{\text{eff}}\dot{V}+\frac{V}{R}=0, \tag{1b}$$

where q is a temporal coordinate representing a measure of the beam's mid-span deflection, V is the output voltage, m is the effective inertia of the first mode, c is a viscous damping coefficient, k is a linear modal stiffness coefficient, P is the static axial load, α is the inverse of critical buckling load, λ is the geometric nonlinearity coefficient, θ is the electromechanical coupling, C_{eff} is the effective capacitance of the piezoelectric layers, R is the electric load, f_1 is a constant representing the projection of the base acceleration onto the first vibration mode, and finally, β is a constant introduced for brevity. All these coefficients are functions of the beam's mode shapes and are further defined in Appendix A.

As described earlier, depending on the value of the buckling load, the beam can exhibit either one or three co-existing equilibrium solutions. These equilibrium solutions are given by

$$q_s = 0, \quad q_s = \pm\sqrt{-\frac{k(1-\alpha P)}{\lambda(1-\beta P)}}. \tag{2}$$

When P is less than the critical buckling load, $1/\alpha$, only the trivial solution, $q_s=0$, exists and the harvester is mono-stable. On the other hand, when P is greater than the critical buckling load, the trivial solution becomes unstable and two nontrivial solutions are born causing the harvester to become of the bi-stable type. Not only does the axial load affects the system's equilibria but it also influences the oscillation frequency around them. To obtain an expression for the local frequency of the harvester about a given equilibrium position, we linearize Eq. (1) around the static equilibria $(q_s, V_s = 0)$. This yields

$$m\ddot{q}_t + c\dot{q}_t + [k(1-\alpha P) + 3\lambda(1-\beta P)q_s^2]q_t + \theta V_t = -mf_1 a_b(t), \tag{3a}$$

$$-\theta\dot{q}_t + C_{\text{eff}}\dot{V}_t + \frac{V_t}{R} = 0, \tag{3b}$$

where $q_t = q - q_s$ and $V_t = V - V_s = V$. With that the frequency of oscillations (short-circuit) around a given equilibrium position can be written as

$$f_0 = \frac{1}{2\pi}\sqrt{\frac{k(1-\alpha P) + 3\lambda(1-\beta P)q_s^2}{m}}. \tag{4}$$

It is worth noting that in the mono-stable configuration, and since $q_s=0$, this expression reverts back to the global frequency of the system. On the other hand, for the bi-stable configuration, the resulting expression represents the oscillation frequency within one of the potential wells.

Fig. 4 depicts both of the experimental and theoretical variations of the oscillation frequency with the axial load. As expected, since the load is compressive, the frequency decreases with the application of the axial load until it reaches

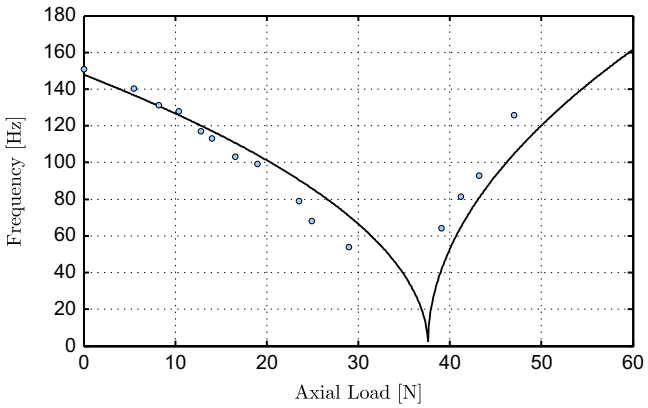

Fig. 4. Variation of the harvester's oscillation frequency (short circuit) with the axial loading. Theoretical (solid line) and experimental (circles).

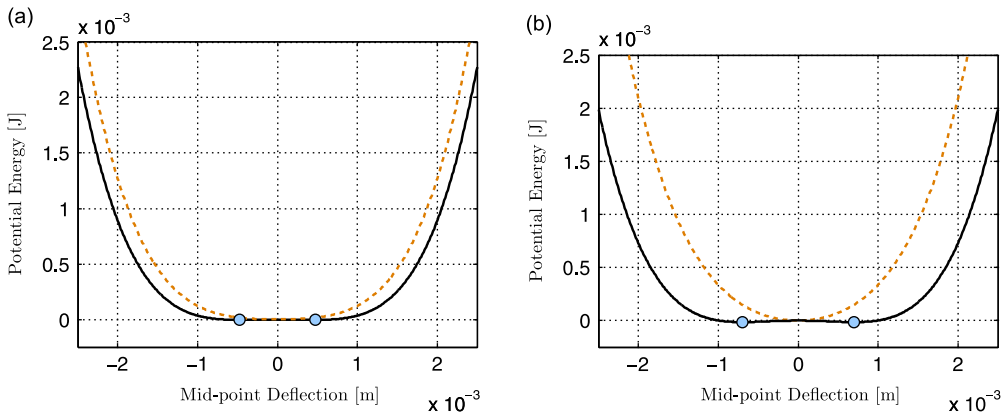

Fig. 5. Potential energy of the harvester at different frequencies (a) f_0=45 Hz and (b) f_0=65 Hz. Bi-stable (solid line), mono-stable (dashed lines), static equilibria (circles).

the critical buckling load which theoretically corresponds to zero frequency. When the beam buckles, the structure stiffens again and the frequency increases. This permits tuning the harvester at equal frequencies for different configurations. For instance, the harvester has an oscillation frequency of 65 Hz in the mono-stable configuration when $P \approx 30$ N, and a frequency (*within one potential well*) of 65 Hz in the bi-stable configuration when $P \approx 43$ N.

The potential energy functions corresponding to equal frequencies and different axial loadings are depicted in Fig. 5(a). For $f_0 = 45$ Hz, the system can have single- or double-well potential functions depending on the value of the axial load. In the bi-stable case, since the axial load is just beyond the critical buckling load, the separation distance between the wells (static equilibria) as well as the height of the potential barrier are very small. This allows the dynamic trajectories to escape from one potential well with small input energy. When f_0 is increased toward 65 Hz, the height of the potential barrier and separation distance between the wells increases. In this case, more energy is required to activate the inter-well dynamics.

3. Comparative investigation

To compare the performance of the harvesters in the mono- and bi-stable configurations, we tune the frequency such that both configurations have the same (local) oscillation frequency. This permits drawing conclusions about their relative behavior for the same frequency range around the same center frequency. In this study, we consider two frequencies; the first when both configurations are tuned to 65 Hz, and the second when both are tuned to 45 Hz, see Fig. 5(a) and (b). Treating these two different cases will also permit comparing the performance of bi-stable harvesters with different potentials.

3.1. Performance when the harvester is tuned to 65 Hz

In this section, we investigate the response of both configurations to harmonic base excitations with a slowly and linearly varying frequency spanning the range between 40 and 90 Hz. Three different base accelerations are considered, namely 7.5, 10, and 14 m/s^2. Variation of the frequency was carried out at a very slow rate such that the resulting curves can be safely considered to represent the steady-state behavior of the system. To further justify that the variation rate is slow enough to be considered quasi-static, the steady-state amplitude was recorded at discrete frequencies and compared to that obtained when the frequency is slowly varied showing negligible differences. Since the system is nonlinear and can exhibit a hysteretic behavior depending on the direction of the frequency sweep, the frequency is swept from low to high values (*forward sweep*) and from high to low values (*reverse sweep*). Experimentally, the excitation signal is generated at a workstation and fed to the harvester using an electrodynamic shaker. The amplitude of oscillation at the beam's mid-span is recorded using a laser vibrometer. For the purpose of comparison under similar electric loading conditions, the voltage is measured across equal 25 kΩ purely resistive loads.[1]

Fig. 6 depicts theoretical variation of the mid-span deflection and output voltage with the frequency for both the mono- and bi-stable configurations in a *forward* sweep at a base acceleration of 7.5 m/s^2. Solid dots represent a bifurcation map generated by simulating Eq. (1) for a very long time for many values of the excitation frequency and collecting points when $\dot{q}(t) = 0$. Close inspection of the results clearly indicates that the response curves bend to the right in the mono-stable case and to the left in the bi-stable configuration. This agrees with our previous findings available in [19] which clearly demonstrate that the effective nonlinearity of the system depends on the axial loading and switches from the *hardening* to the *softening* type beyond the critical buckling load. We can also observe that, in the bi-stable configuration, oscillations remain, for the most part, confined to one potential well except for a small frequency range near 52 Hz where a chaotic inter-well behavior is activated. This implies that the base acceleration is not large enough to activate the inter-well dynamics over a large frequency range. Consequently, the resulting dynamic behavior remains of the resonant intra-well nature and the voltage remains very small. In such a scenario, operating the harvester in the bi-stable configuration does not provide any enhancement in the output voltage. This becomes evident when comparing the output voltage of both harvesters as depicted in Fig. 6(a) and (b).

Similar behavior can also be seen in the experimental results shown in Fig. 7 for both the mono- and bi-stable configurations. In the mono-stable scenario, we observe similar bend in the frequency–response curves, with the jump from the higher branch to the lower branch of solutions occurring at a smaller value of the excitation frequency. This is generally expected because it is harder to maintain oscillations near the higher energy branch of solutions in an experimental setting. The bi-stable results also demonstrate that the dynamics remain confined to a single well limiting the amplitude of the output voltage.

We do not observe much differences in the *reverse* frequency sweep (Figs. 8 and 9). As expected, the jump from the lower branch to the higher branch of solutions occurs at a lower value of the excitation frequency for the mono-stable configuration, and from the higher branch to the lower branch in the bi-stable configuration. With small exception near

[1] Since, in general, the effect of the electric load can be well approximated by a linear electric damping term, the comparison can be carried at any electric load provided it is kept constant in both configurations to produce equal linear damping.

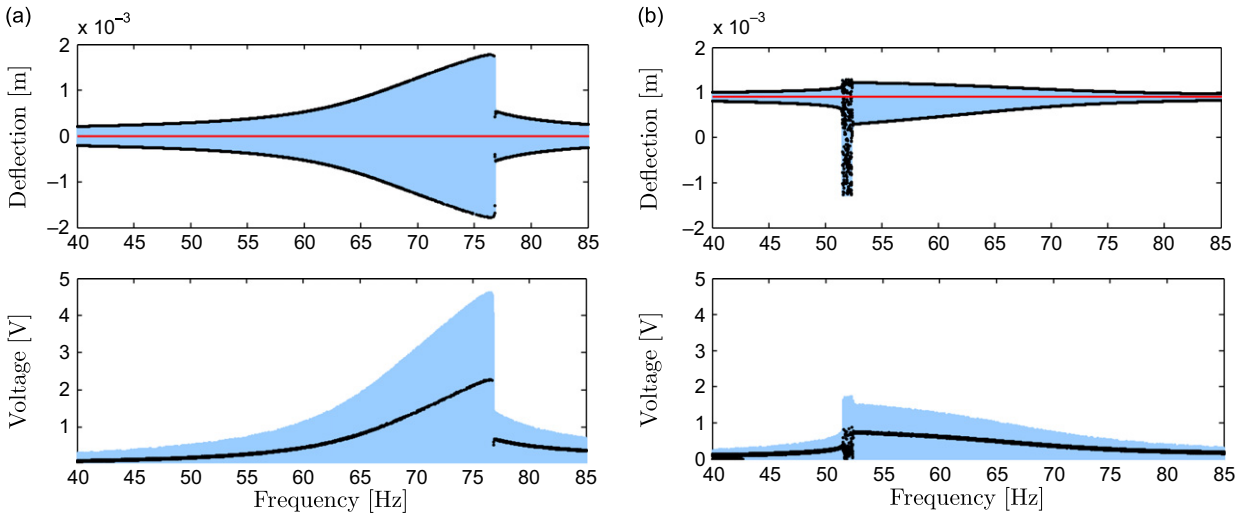

Fig. 6. (*Forward sweep*) Theoretical forward frequency response curves for a base excitation of 7.5 m/s^2: (a) mono-stable and (b) bi-stable. Black dots represent a bifurcation map and solid horizontal (red) lines represent the stable equilibria. (For interpretation of the references to color in this figure legend, the reader is referred to the web version of this article.)

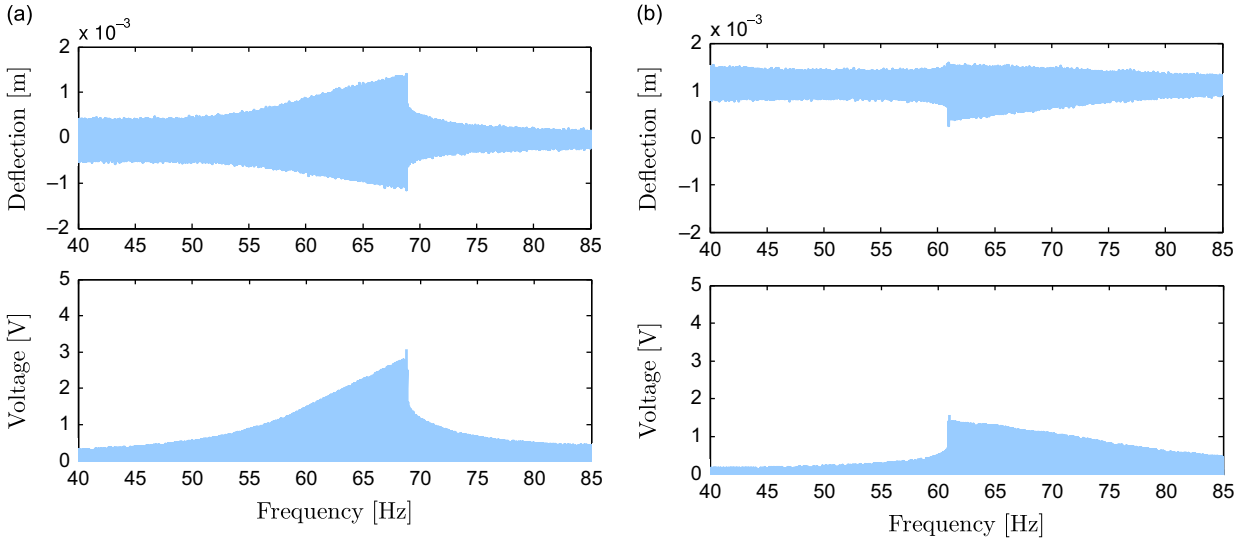

Fig. 7. (*Forward sweep*) Experimental forward frequency response curves for a base excitation of 7.5 m/s^2: (a) mono-stable and (b) bi-stable.

49 Hz, the oscillations remain confined to one potential well in the bi-stable scenario. Experimental results demonstrate similar behavior over the whole frequency range.

When the amplitude of input acceleration is increased to 10 m/s^2, the response of the mono-stable harvester remains generally the same in the *forward* and *reverse* sweeps. The only notable difference, as shown in Figs. 10(a) and 12(a), is that the amplitude of the mid-span deflection and output voltage increases and that the higher branch of solutions extends over a wider range of frequencies. The same behavior is also observed experimentally in Figs. 12 and 13.

In the bi-stable configuration, except in the region between 48 and 58 Hz, a forward sweep yields oscillations that remain confined to one potential well limiting the amplitude of the harvester's output voltage as shown in Fig. 10(b). Between 48 and 58 Hz, chaotic inter-well dynamic response is activated causing the output voltage to grow. This is also observed experimentally in Fig. 11(b). However, in general, for the most part of the frequency range considered, the mono-stable harvester still clearly outperforms the bi-stable one.

In the reverse sweep shown in Fig. 12(b), we observe that the region of chaotic inter-well dynamics is now preceded by a region of periodic large-amplitude inter-well oscillations (limit cycles) which are very desirable for energy harvesting. These oscillations exist only in the lower range of the frequency spectrum producing large output voltage at these

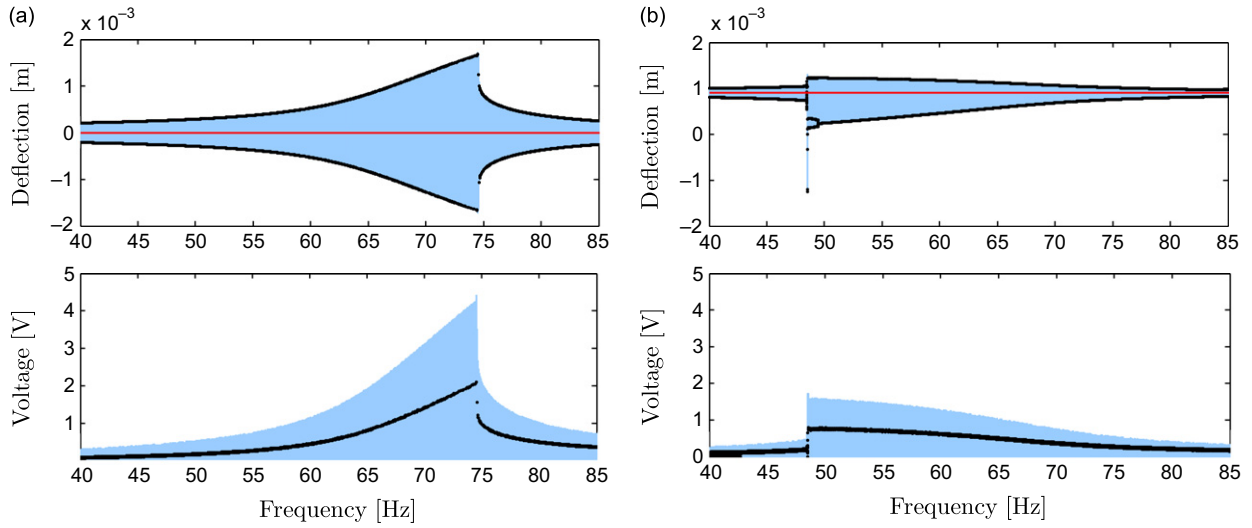

Fig. 8. (*Reverse sweep*) Theoretical reverse frequency response curves for a base excitation of 7.5 m/s^2: (a) mono-stable and (b) bi-stable. Black dots represent a bifurcation map and solid horizontal (red) lines represent the stable equilibria. (For interpretation of the references to color in this figure legend, the reader is referred to the web version of this article.)

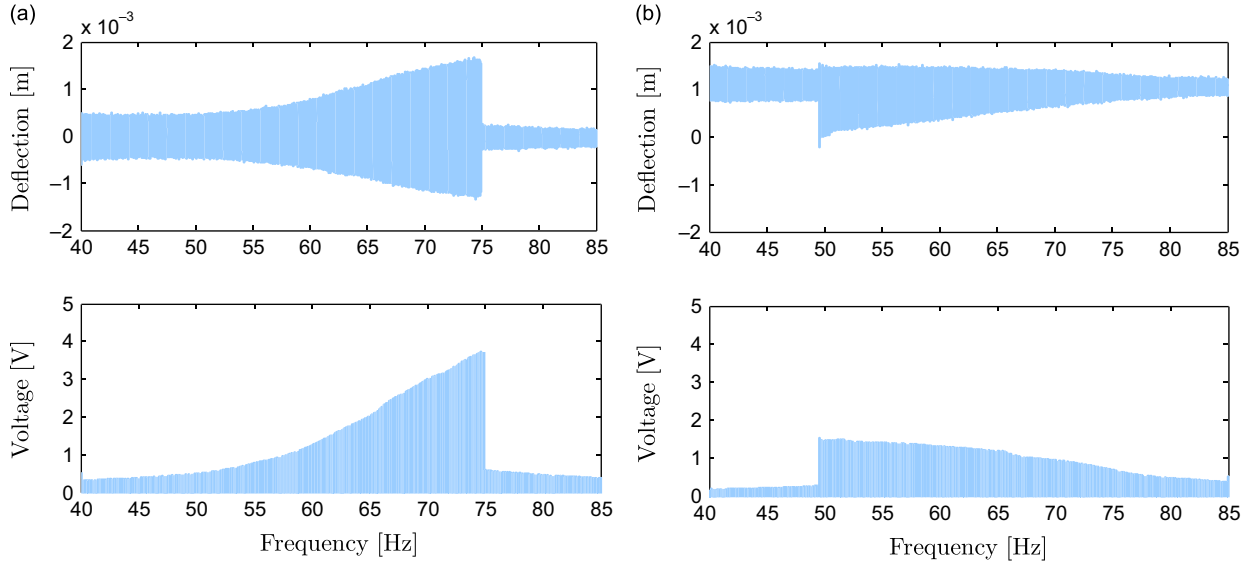

Fig. 9. (*Reverse sweep*) Experimental reverse frequency response curves for a base excitation of 7.5 m/s^2: (a) mono-stable, and (b) bi-stable.

frequencies and causing the bi-stable harvester to outperform the mono-stable one in the lower frequency range. Similar behavior is also observed experimentally in Fig. 13.

When the acceleration amplitude is increased to 14 m/s^2, a forward frequency sweep can now excite the inter-well periodic oscillations over a much wider range of frequencies as shown in Fig. 14(b). This results in a large voltage output over a wide frequency spectrum ranging between 43 and 78 Hz. As a result, the bi-stable harvester outperforms the mono-stable one over most of the frequency range considered, see Fig. 14(a). Similar trends are also demonstrated experimentally in Fig. 15(b). However, in the experimental settings the inter-well oscillations were only confined to a smaller range of the frequency spectrum (46–66 Hz).

As depicted in Fig. 16(b), in the reverse sweep, the oscillations of the bi-stable harvester remain confined to one potential well over the higher range of frequencies. As such, the mono-stable harvester provides higher power levels over that frequency range (62–90 Hz). When the excitation frequency approaches 62 Hz, the bi-stable harvester undergoes complex dynamic responses characterized by chaotic inter-well oscillations and windows of period-doubling bifurcations as shown in Fig. 16(b). This complex behavior continues until the frequency reaches 52 Hz, where the inter-well dynamics become large and periodic causing the output voltage to increase significantly. As a result, the bi-stable harvester

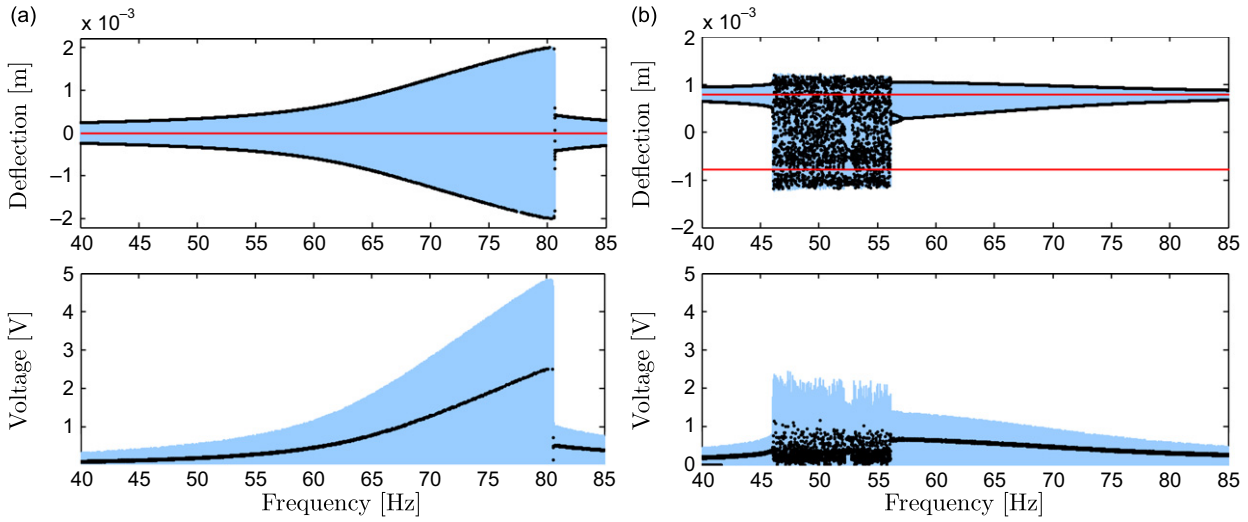

Fig. 10. (*Forward sweep*) Theoretical forward frequency response curves for a base excitation of 10 m/s^2: (a) mono-stable and (b) bi-stable. Black dots represent a bifurcation map and solid horizontal (red) lines represent the stable equilibria. (For interpretation of the references to color in this figure legend, the reader is referred to the web version of this article.)

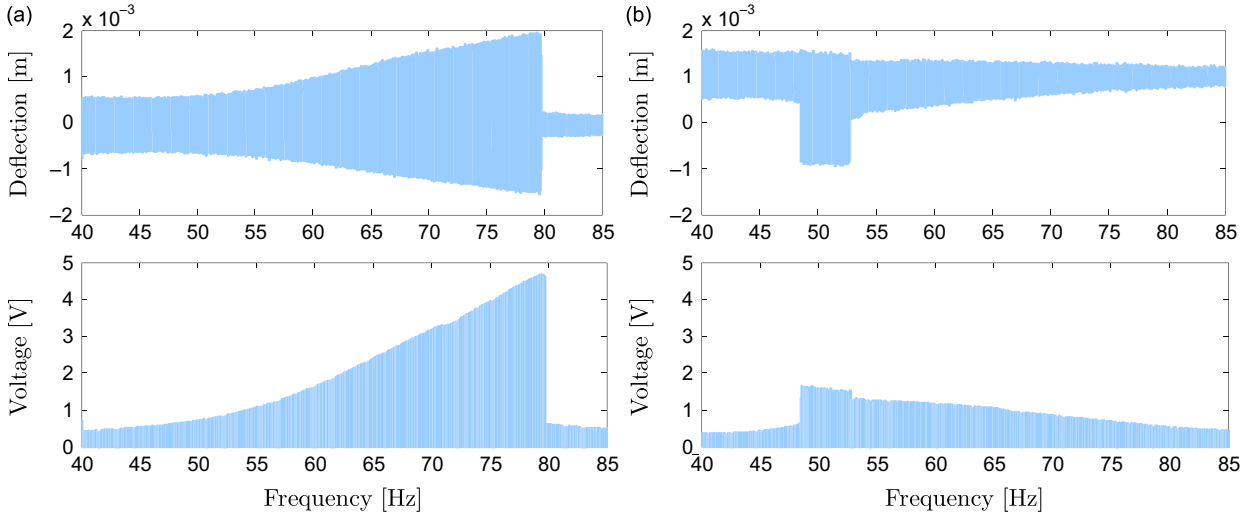

Fig. 11. (*Forward sweep*) Experimental forward frequency response curves for a base excitation of 10 m/s^2: (a) mono-stable and (b) bi-stable.

outperforms the mono-stable one for the lower range of frequencies. This behavior can also be clearly observed in the experimental results shown in Fig. 17.

3.2. *Performance when the harvester is tuned to 45 Hz*

In this section, we tune both configurations to a frequency of 45 Hz which corresponds to buckling loads that are very close to the critical buckling load, see Fig. 4. At this frequency, the bi-stable configuration has a potential function with very shallow and closely separated wells. Consequently, as shown in Fig. 5(a), the bi-stable potential appears very similar to the mono-stable one. Again, we investigate the response of both configurations to harmonic base excitations with a slowly and linearly varying frequency spanning the range between 10 and 100 Hz. Two base accelerations are considered, namely 7.5 m/s^2, and 14 m/s^2. Since the model has been experimentally validated in both of the static and dynamic cases, and in the mono- and bi-stable scenarios for different acceleration levels and in both directions of the frequency sweep, only the theoretical results are presented in this section.

Fig. 18 depicts variation of the mid-span deflection and output voltage for a forward sweep with base acceleration of 7.5 m/s^2. The behavior of the mono-stable configuration remains the same with the frequency response curves bending to

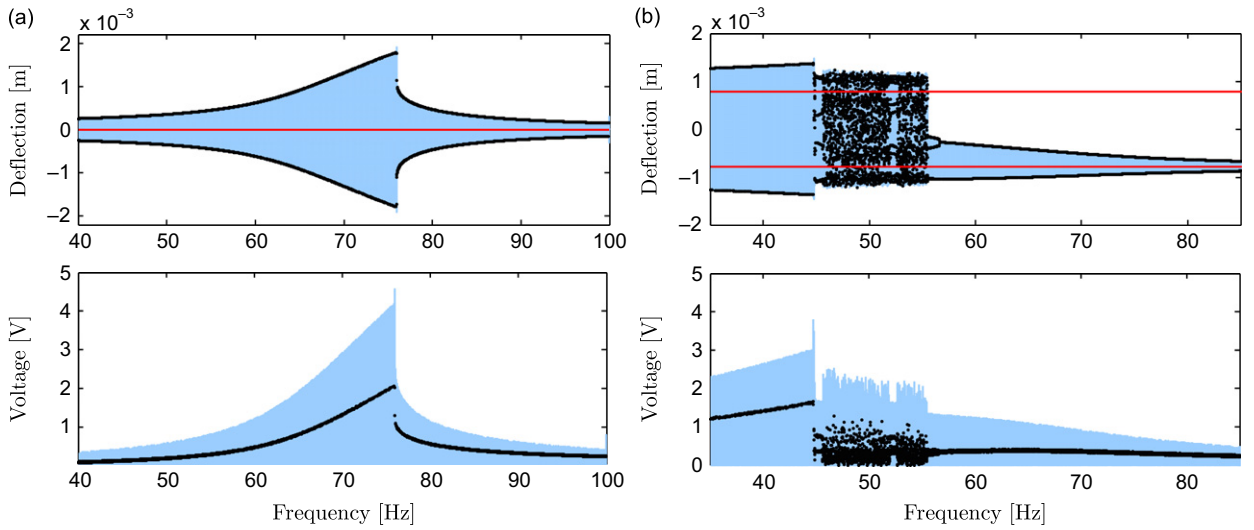

Fig. 12. (*Reverse sweep*) Theoretical reverse frequency response curves for a base excitation of 10 m/s^2: (a) mono-stable and (b) bi-stable. Black dots represent a bifurcation map and solid horizontal (red) lines represent the stable equilibria. (For interpretation of the references to color in this figure legend, the reader is referred to the web version of this article.)

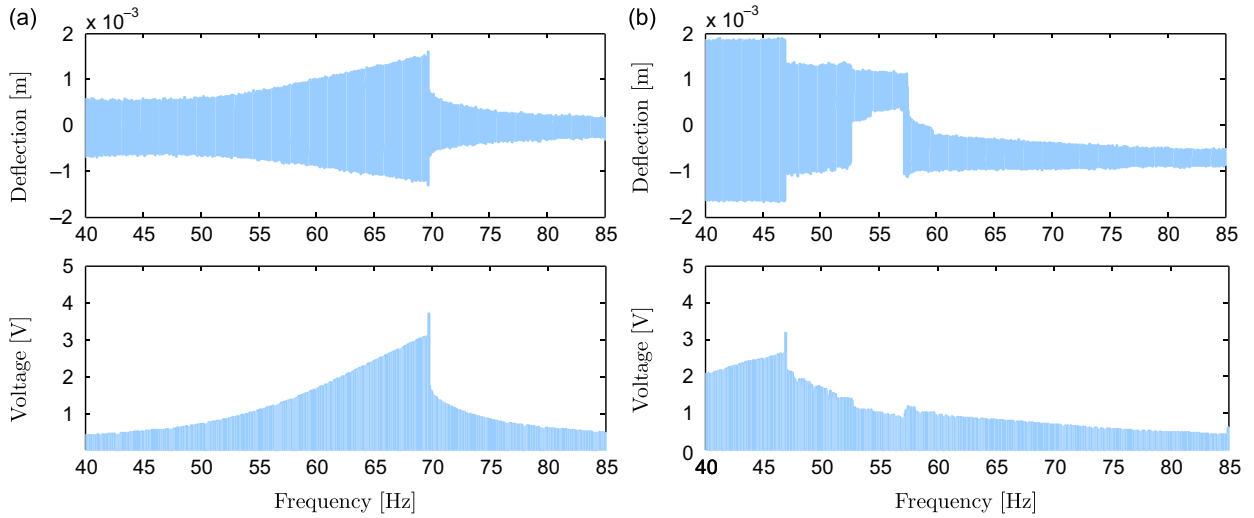

Fig. 13. (*Reverse sweep*) Experimental reverse frequency response curves for a base excitation of 10 m/s^2: (a) mono-stable and (b) bi-stable.

the right due to the hardening-type nonlinearity. When compared to the 65 Hz case depicted earlier in Fig. 6, it can be seen that the magnitude of the output voltage is generally larger. This is expected because, for the larger axial load, the structure is softer and same input acceleration yields larger deflections, see [19] for more details. Unlike when the harvester was tuned at 65 Hz, the small input acceleration can activate the inter-well periodic oscillations in the bi-stable configuration. This stems from the shallow nature of the potential wells in this case. As a result, even for small input accelerations, the bi-stable harvester can provide large output voltage over a wide bandwidth of frequencies. However, as seen in Fig. 18, in general the mono-stable design can still provide comparable voltage outputs even for most of the range where the inter-well limit-cycle behavior is activated.

We also note that, in the case of this shallow bi-stable potential, secondary resonances (super- and sub-harmonics) of order two and three can activate chaotic dynamic responses, see the regions near 15, 22.5 and 90 Hz in Fig. 18(b). Such super- and sub-harmonics do not seem to produce large amplitude responses in the mono-stable scenario.

The effect of the super-harmonics becomes even more evident in the reverse sweep as shown in Fig. 19(b). Indeed, oscillations resulting from the super-harmonic resonance combine with those resulting from the primary resonance to

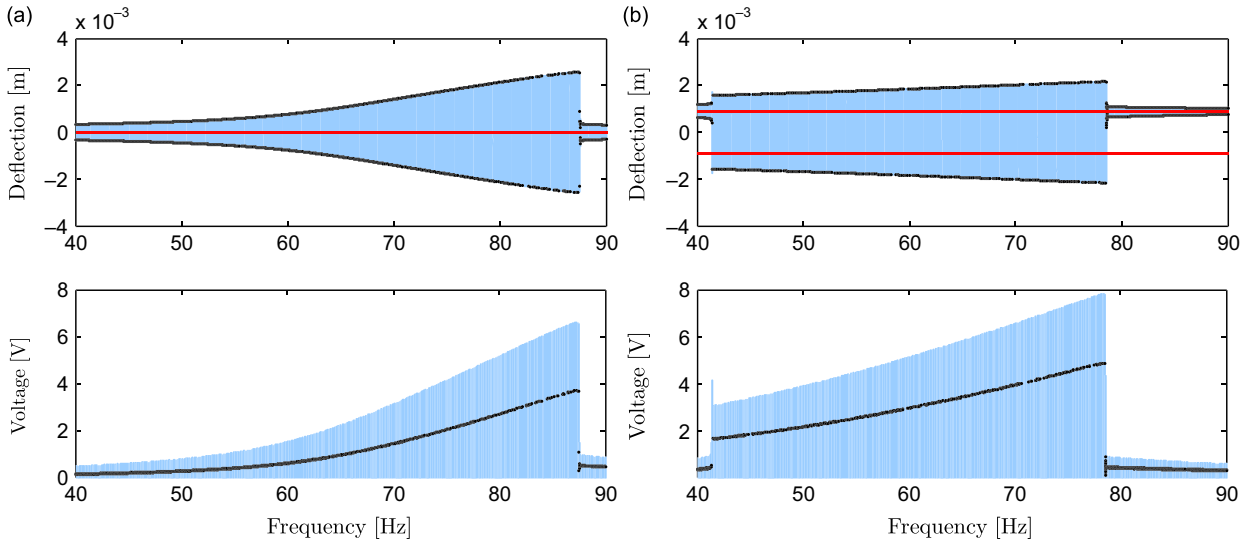

Fig. 14. (*Forward sweep*) Theoretical forward frequency response curves for a base excitation of 14 m/s^2: (a) mono-stable and (b) bi-stable. Black dots represent a bifurcation map and solid horizontal (red) lines represent the stable equilibria. (For interpretation of the references to color in this figure legend, the reader is referred to the web version of this article.)

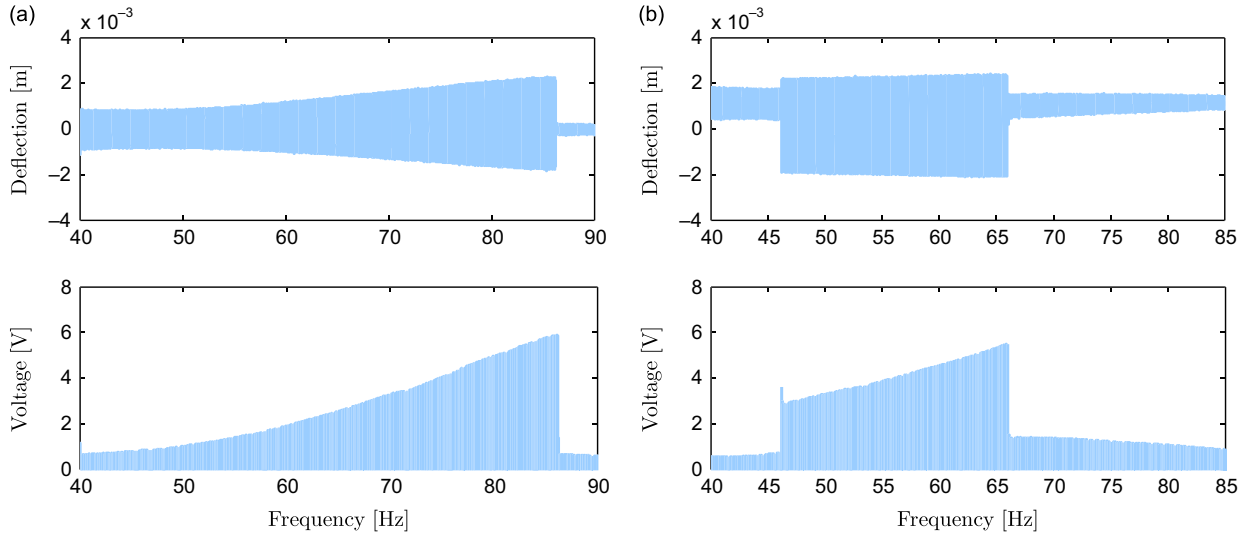

Fig. 15. (*Forward sweep*) Experimental forward frequency response curves for a base excitation of 14 m/s^2: (a) mono-stable and (b) bi-stable.

provide a large and continuous region of inter-well oscillations in the frequency domain. As a result, the bi-stable harvester outperforms the mono-stable one over the lower range of frequencies.

When the base acceleration in increased to 14 m/s^2, a forward frequency sweep reveals that the inter-well dynamics is activated over the whole frequency domain, see Fig. 20(b). The resulting dynamics is mostly periodic except for a small region near the super-harmonic resonances. We also observe striking similarities between the response of the mono- and bi-stable harvesters in the forward sweep. When the input acceleration is large enough, the inter-well oscillations of the bi-stable system can always be activated near the primary resonance. As such, since the potential functions associated with the mono- and bi-stable configurations are very similar in shape near the critical buckling load, their global dynamic behavior exhibits striking similarities as can be clearly seen in the figure. The main difference between the two responses appears in the vicinity of the system's super-harmonic resonances. Specifically, we note that super-harmonic resonances of order two and three activate complex inter-well oscillations in the bi-stable configuration. Such resonances require very large input energy to appear in the mono-stable scenario. The reverse sweep associated with the 14 m/s^2 case demonstrates similar findings and is depicted in Fig. 21.

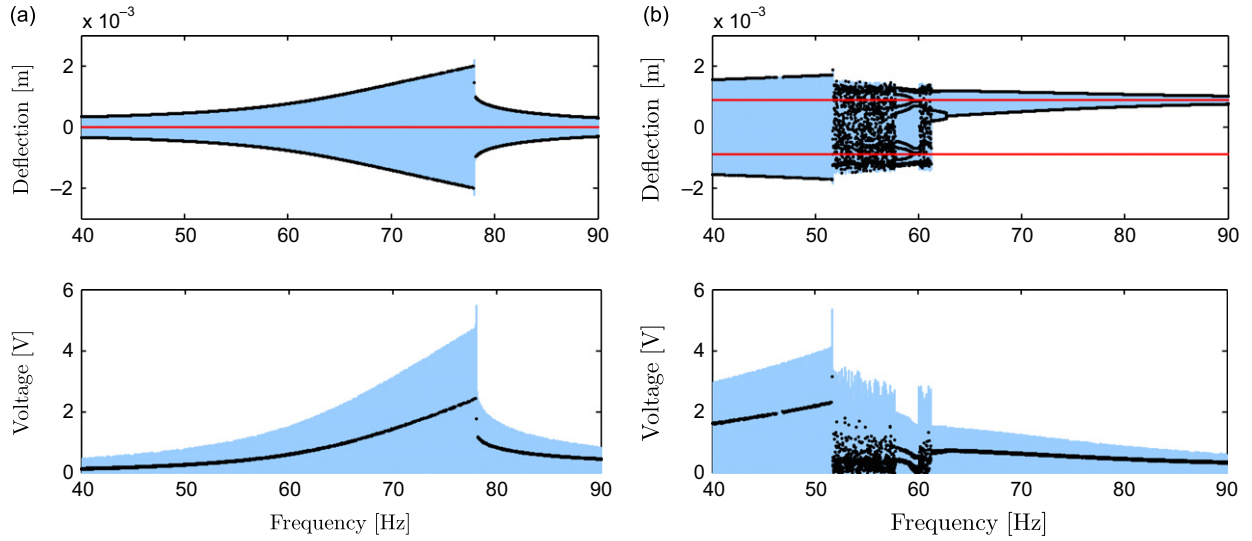

Fig. 16. (*Reverse sweep*) Theoretical reverse frequency sweep response for a base excitation of 14 m/s^2: (a) mono-stable and (b) bi-stable. Black dots represent a bifurcation map and solid horizontal (red) lines represent the stable equilibria. (For interpretation of the references to color in this figure legend, the reader is referred to the web version of this article.)

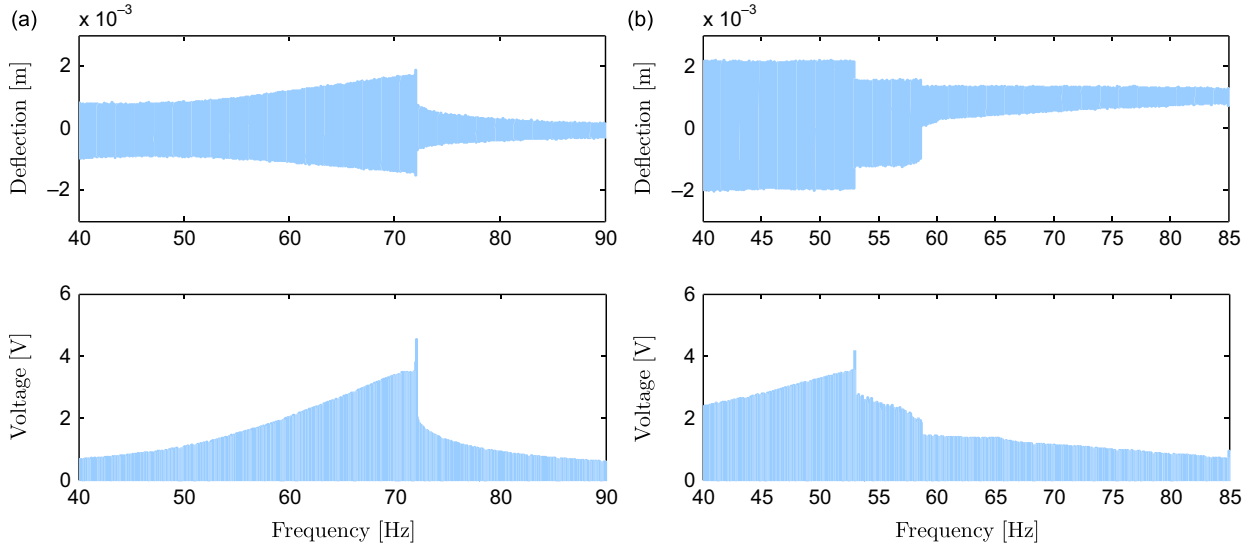

Fig. 17. (*Reverse sweep*) Experimental reverse frequency sweep response for a base excitation of 14 m/s^2: (a) mono-stable and (b) bi-stable.

4. Conclusions

The theoretical and experimental results presented in the previous sections permit making general observations and drawing conclusions about the relative performance of nonlinear harvesters in mono- and bi-stable potentials. In contrast to the common understanding that a bi-stable harvester has a wider bandwidth of large amplitude voltages as compared to the mono-stable design, this paper clearly illustrates that this enhanced bandwidth is very much dependent on the level of input acceleration and the shape of the bi-stable potential function. Indeed, many of the presented scenarios clearly demonstrate the mono-stable harvester can outperform the bi-stable one. Following is a more detailed summary of the main observations:

- When the harvester is subjected to base accelerations of small magnitude, the mono-stable harvester outperforms the bi-stable harvester with the deeper potential wells over most of the frequency domain and in both directions of the frequency sweep. This is due to the inability of the base excitation to activate the inter-well dynamics in the bi-stable case. As such, dynamic trajectories remain confined to a single potential well limiting the output voltage of the harvester in the bi-stable configuration.

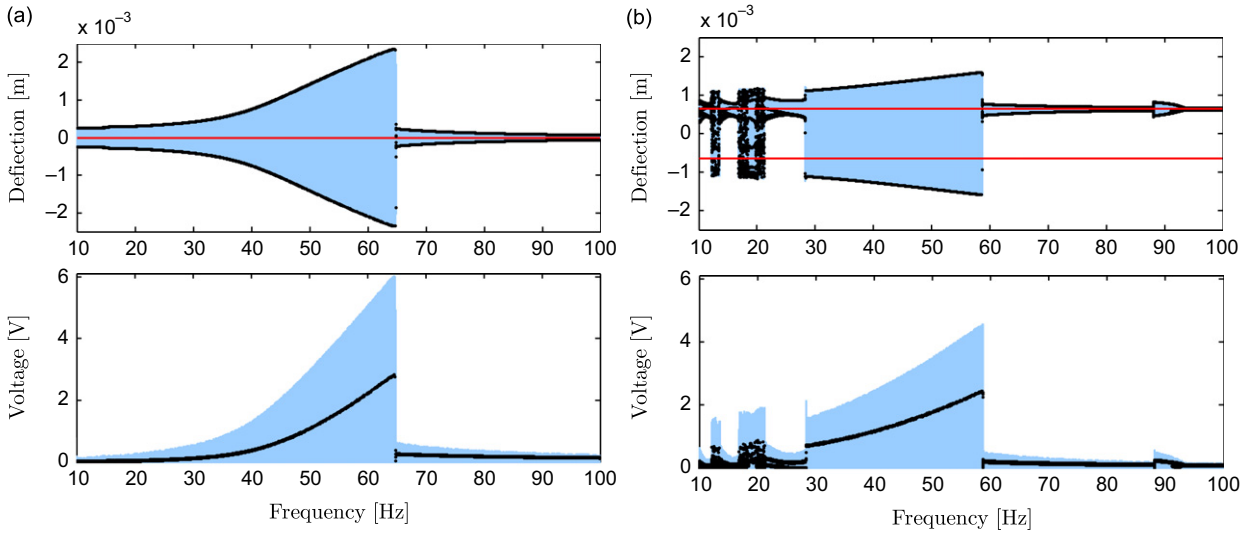

Fig. 18. (*Forward sweep*) Theoretical forward frequency response curves for a base excitation of 7.5 m/s^2: (a) mono-stable and (b) bi-stable. Black dots represent a bifurcation map and solid horizontal (red) lines represent the stable equilibria. (For interpretation of the references to color in this figure legend, the reader is referred to the web version of this article.)

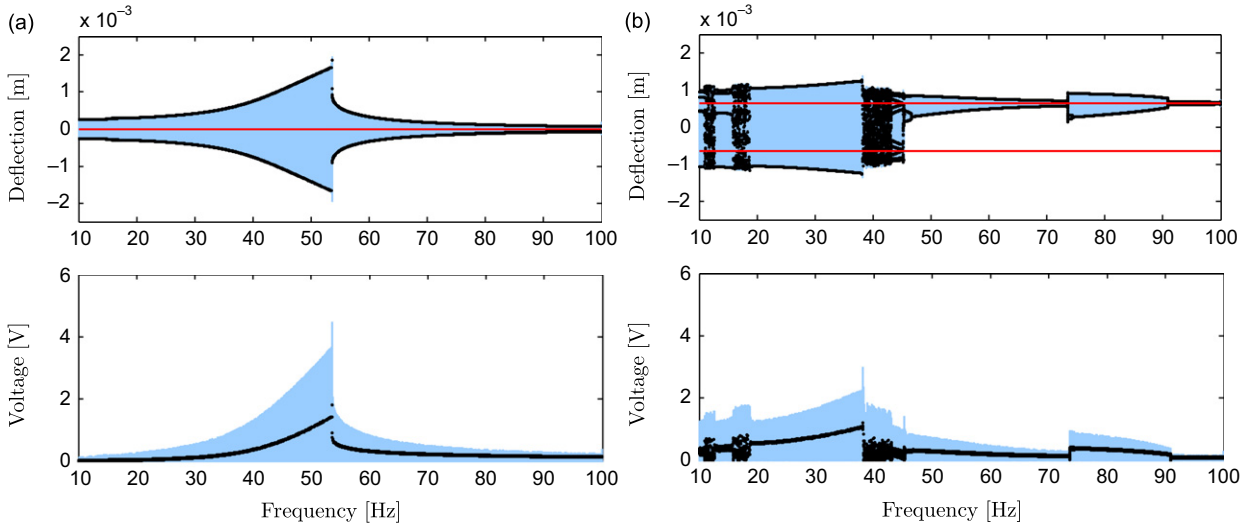

Fig. 19. (*Reverse sweep*) Theoretical reverse frequency response curves for a base excitation of 7.5 m/s^2: (a) mono-stable and (b) bi-stable. Black dots represent a bifurcation map and solid horizontal (red) lines represent the stable equilibria. (For interpretation of the references to color in this figure legend, the reader is referred to the web version of this article.)

- As the magnitude of the input acceleration is sufficiently increased to activate the inter-well dynamics for the deeper bi-stable potential, it can in some instances outperform the mono-stable design. Enhancement is mostly pronounced for the lower range of excitation frequencies and away from the primary resonance of both harvesters (tuned frequency). However, no clear results point toward significant enhancements around the primary tuned resonance.
- For the bi-stable potential with shallow potential wells, inter-well dynamics can be excited even for small input accelerations. However, because of the general similarities between the mono- and bi-stable potentials in this case, the resulting output voltage near the primary resonance appears to be of comparable magnitude for both configurations. As such, one cannot make the claim that the bi-stable harvester can outperform the mono-stable one near the tuned frequency. On the other hand, it is observed that secondary resonances can activate the inter-well dynamics in the case of a shallow bi-stable potential, thereby causing the bi-stable harvester to outperform the mono-stable one in their vicinity.
- As the input acceleration is increased for the shallow bi-stable configuration, we observe striking similarities between the response amplitude and behavior of both harvesters especially in the forward frequency sweep and near the tuned

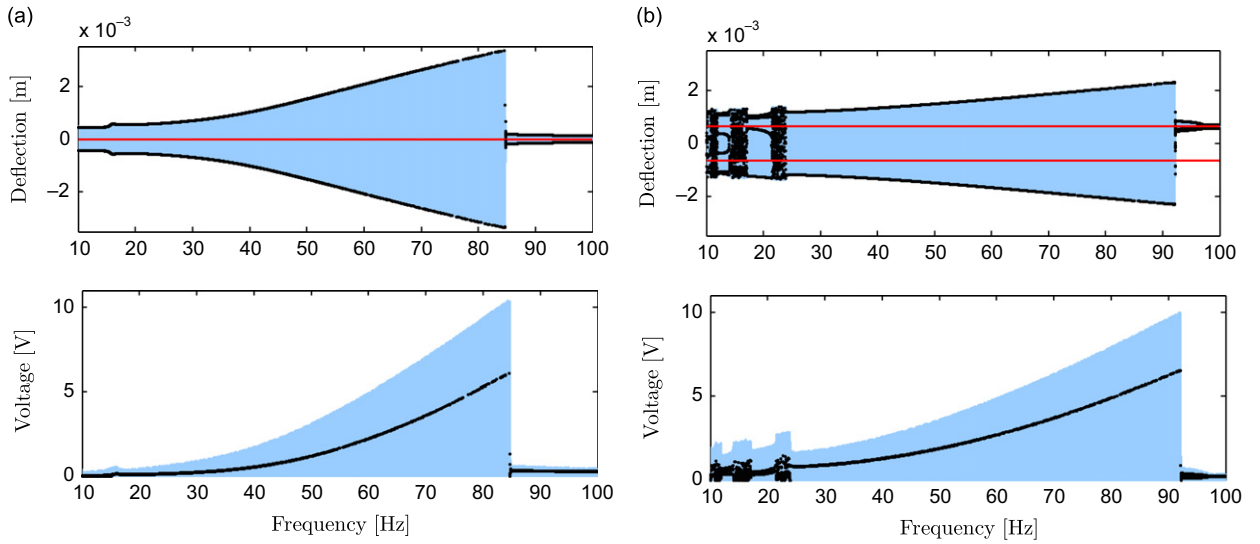

Fig. 20. (*Forward sweep*) Theoretical forward frequency response curves for a base excitation of 14 m/s^2: (a) mono-stable and (b) bi-stable. Black dots represent a bifurcation map and solid horizontal (red) lines represent the stable equilibria. (For interpretation of the references to color in this figure legend, the reader is referred to the web version of this article.)

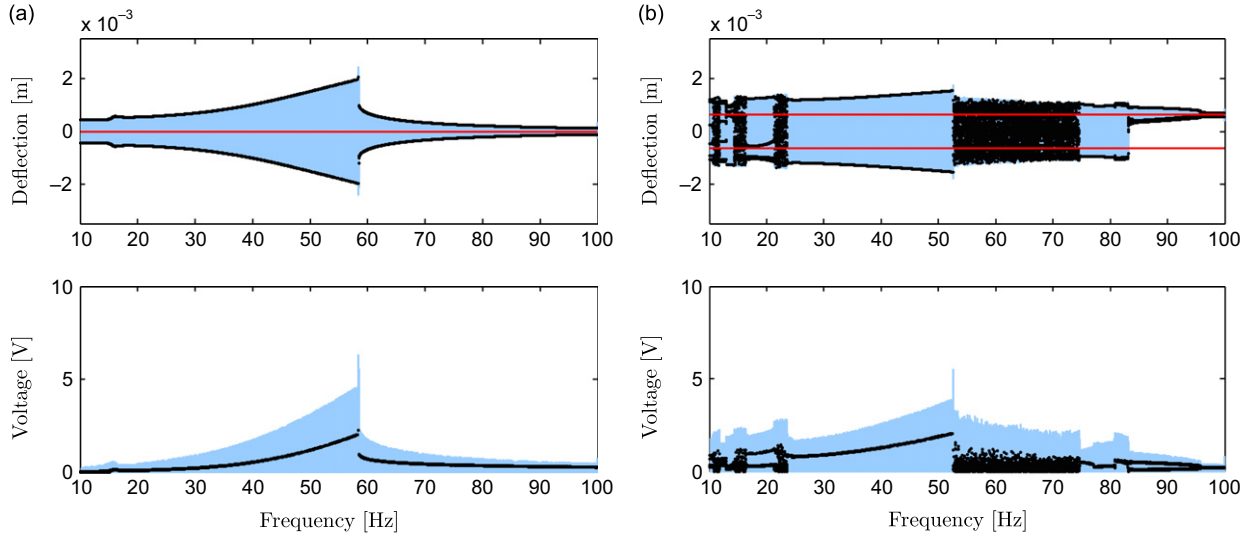

Fig. 21. (*Reverse sweep*) Theoretical reverse frequency response curves for a base excitation of 14 m/s^2: (a) mono-stable and (b) bi-stable. Black dots represent a bifurcation map and solid horizontal (red) lines represent the stable equilibria. (For interpretation of the references to color in this figure legend, the reader is referred to the web version of this article.)

frequency. Again, this is attributed to the similarity of their potential shapes. However, because secondary resonances, both super- and sub-harmonic, can be easily activated in the bi-stable scenario, one can safely conclude that the bi-stable harvester outperforms the mono-stable one especially in their vicinity.

With these observations, it is possible to conclude that the relative performance of mono- and bi-stable harvesters is dependent on the shape of the potential functions in the bi-stable case in conjunction with the input acceleration. Generally, for a bi-stable potential with deep and widely separated wells, large input accelerations are essential to produce voltages that are comparable or larger in magnitude than those obtained in the mono-stable scenario. Even under these conditions, enhancement in the output voltage seems to be limited to the lower frequency range and away from the tuned primary frequency of the system. When the potential wells are shallow and closely separated, the inter-well dynamics can be easily excited even for small input acceleration. However, the resulting voltage seems to be of comparable size to that obtained in the mono-stable case. When the magnitude of input acceleration becomes large enough to guarantee inter-well oscillations over the whole frequency spectrum, the bi-stable harvester with the shallow potential produces almost

similar output voltage to the mono-stable design near and around the primary frequency. However, due to the activation of secondary resonances in the bi-stable case, the bi-stable harvester outperforms the mono-stable design for the lower and higher range of frequencies.

Acknowledgments

The authors would like to acknowledge the generous support of the National Science Foundation (NSF) through NSF CAREER grant CMMI-1055419 "CAREER: Electromechanical Transduction of Vibratory Energy Harvesters in Random and Non-Stationary Environments". Any opinions, findings, and conclusions or recommendations expressed in this material are those of the authors and do not necessarily reflect the views of the National Science Foundation.

Appendix A. Derivation of the equations of motion

A detailed derivation of the governing equations of an axially loaded energy harvester is available in [19]. A brief summary of the derivations is available here. To derive the governing equations, we use Hamilton's principle in conjunction with the nonlinear Euler–Bernoulli's beam theory. Respectively, the kinetic and potential energies of the system can be expressed as

$$T = \int_{\mathcal{V}_s} \frac{1}{2}\rho_s(\dot{u}^2+\dot{w}^2)\,\mathrm{d}\mathcal{V}_s + \int_{\mathcal{V}_p} \frac{1}{2}\rho_p(\dot{u}^2+\dot{w}^2)\,\mathrm{d}\mathcal{V}_p, \tag{A.1a}$$

$$U = \frac{1}{2}\int_{\mathcal{V}_s} \sigma_s\varepsilon_s\,\mathrm{d}\mathcal{V}_s + \frac{1}{2}\int_{\mathcal{V}_p} \sigma_p\varepsilon_p\,\mathrm{d}\mathcal{V}_p - \frac{1}{2}\int_{\mathcal{V}_p} E_pD_p\,\mathrm{d}\mathcal{V}_p, \tag{A.1b}$$

where the over-dots denote derivatives with respect to time, t; u and w are, respectively, the longitudinal and transversal deflection of the beam; $\mathcal{V}$ represents the domain; ρ is the mass density per unit length; σ denotes the stress, ε denotes the strain; E denotes the electric field; D is the electric displacement; and the subscripts s and p are used to represent properties associated with the structural and piezoelectric layers, respectively. Using the linear constitutive equations of piezoelectricity, the stress, σ, and electric displacement, D, can be further related to the resulting strain, ε, according to

$$\sigma_p = C_p\varepsilon_p(s,z,t) - e_{31}E_p, \quad D_p = e_{31}\varepsilon_p(s,z,t) + \epsilon E_p, \quad \sigma_s = C_s\varepsilon_s(s,z,t), \tag{A.2}$$

where C is the Young's modulus at constant electric field, e_{31} is the piezoelectric constant, ϵ is the permittivity at constant strain, and E_p is the electric field which can be related to the voltage, $V(t)$, developed across the piezoelectric layer of thickness, t_p, using $E_p = V(t)/t_p$. Using the nonlinear Euler–Bernoulli beam theory, the total strain, $\varepsilon(s,z,t)$, developed in a differential beam element located at a distance z from the neutral axis of the beam can be written as

$$\varepsilon(s,z,t) = u' + \frac{w'^2}{2} - \frac{w'^4}{8} - \frac{u'w'^2}{2} - z\left(w'' - 2w''u' - w'u'' - \frac{3}{2}w'^2w''\right), \tag{A.3}$$

where the over-primes are derivatives with respect to the arclength, s. The total non-conservative virtual work done by the transversal external acceleration $a_b(t)$, the external axial load, P, the damping forces, as well as the work done to extract the electric energy can be expressed collectively as

$$\delta W^{nc} = \int_0^L a_b(t)\delta w(s,t)\,\mathrm{d}s + \int_0^L c_1\dot{w}\delta w(s,t)\,\mathrm{d}s - P\delta u(L,t) + Q\delta V(t), \tag{A.4}$$

where δ is a variational operator, Q represents the extracted charge, and c_1 is a viscous damping coefficient. Eqs. (A.1)–(A.4) are then substituted into Hamilton's principle to obtain the equations governing the motion of the electromechanical system which is described by the longitudinal deflection, $u(s,t)$, the transversal deflection, $w(s,t)$, and the output voltage, $V(t)$. Since the beam is slender, the longitudinal inertia and flexural rigidity are negligibly small compared to the axial rigidity and are hence neglected. This permits eliminating the longitudinal dynamics of the beam by expressing it in terms of the transversal deflection according to

$$u'(s,t) = -\frac{P}{k_a} - \frac{w'^2}{2}, \tag{A.5}$$

where $k_a = C_sA_s + (H_{L_1} - H_{L_2})C_pA_p$. Here, A denotes the cross-sectional area, and $H_x \equiv H(s-x)$ is the Heaviside function. The resulting equations in $w(s,t)$ and $V(t)$ are then discretized using a Galerkin expansion. This can be achieved by expressing the spatio-temporal function $w(s,t)$ in the form of a series of a linear combination of admissible function that are functions of the spatial coordinates multiplied by unknown temporal functions in the form:

$$w(s,t) = \sum_{i=1}^{\infty} \phi_i(s)q_i(t), \tag{A.6}$$

where $q_i(t)$ are the generalized temporal coordinates and $\phi_i(s)$ are chosen as the set of orthonormal admissible functions representing the mode shapes of a clamped–clamped beam. Assuming that the mid-span static deflection of the beam is small in the bi-stable case and that the excitation frequency is always close to the frequency of the first mode which is assumed to be free of any internal resonances or any external combination resonance with any of the other higher vibration modes, we can adopt a single-mode approximations of the system dynamics. This yields

$$m\ddot{q}+c\dot{q}+k(1-\alpha P)q+\lambda(1-\beta P)q^3+\theta V=-mf_1a_b(t), \tag{A.7a}$$

$$-\theta\dot{q}+C_{\text{eff}}\dot{V}+\frac{V}{R}=0, \tag{A.7b}$$

where

$$m=\int_0^L M\phi^2(s)\,\mathrm{d}s,\quad c=\int_0^L c_1\phi^2(s)\,\mathrm{d}s,\quad k=\int_0^L k_b\phi''^2(s)\,\mathrm{d}s,$$

$$\alpha=\frac{1}{k}\int_0^L \phi'^2(s)\,\mathrm{d}s,\quad \lambda=\int_0^L k_b\phi'^2(s)\phi''^2(s)\,\mathrm{d}s,\quad \beta=\frac{1}{2\lambda}\int_0^L \phi'^4(s)\,\mathrm{d}s,$$

$$\theta=-\int_0^L 2\vartheta\phi''(s)\,\mathrm{d}s,\quad f_1=\int_0^L \phi(s)\,\mathrm{d}s,\quad C_{\text{eff}}=\frac{1}{2}\int_0^L \mathcal{C}(s)\,\mathrm{d}s,$$

and

$$M=\rho_sA_s+(H_{L_1}-H_{L_2})\rho_pA_p,\quad \vartheta=(H_{L_1}-H_{L_2})\frac{e_{31}J_p}{t_p},$$

$$k_b=C_sI_s+(H_{L_1}-H_{L_2})C_pI_p,\quad \mathcal{C}=(H_{L_1}-H_{L_2})\frac{\epsilon A_p}{t_p^2},$$

$$I_p=\frac{b_pt_p}{3}\left(t_p^2+\frac{3t_s}{2}(t_s+t_p)\right),\quad J_p=\frac{b_p}{2}(t_p^2+t_st_p),$$

$$I_s=\frac{b_st_s^3}{12},\quad A_s=b_st_s,\quad A_p=b_pt_p. \tag{A.8}$$

Here, t denotes the thickness and b denotes the width with the subscripts p and s again representing, respectively, the piezoelectric and structural layers.

References

[1] J.W. Kim, H. Takao, K. Sawada, M. Ishida, Integrated inductors for RF transmitters in CMOS/MEMS smart microsensor systems, *Sensors* 7 (2007) 1387–1398.

[2] S. Gregori, Y. Li, H. Li, J. Liu, F. Maloberti, 2.45 GHz power and data transmission for a low-power autonomous sensors platform, in: *International Symposium on Low Power Electronics and Design, ISLPED 04*, 2004, pp. 269–273.

[3] D.J. Inman, B.L. Grisso, Towards autonomous sensing, *Proceedings of Smart Structures and Materials Conference*, SPIE, San Diego, CA, 2006, p. 61740T.

[4] K. Baerta, B. Gyselinckxa, T. Torfsa, V. Leonova, F. Yazicioglua, S. Brebelsa, S. Donnaya, J. Vanfleterena, E. Beyna, C.V. Hoof, Technologies for highly miniaturized autonomous sensor newtorks, *Microelectronics Journal* 37 (2006) 1563–1568.

[5] W. Bracke, P. Merken, R. Puers, C.V. Hoof, Generic architectures and design methods for autonomous sensors, *Sensors and Actuators A* 135 (2007) 881–888.

[6] S. Roundy, P.K. Wright, J. Rabaey, A study of low level vibrations as a power source for wireless sensor nodes, *Computer Communciations* 26 (2003) 1131–1144.

[7] S. Roundy, P.K. Wright, A piezoelectric vibration-based generator for wireless electronics, *Journal of Intelligent Materials and Structures* 16 (2005) 809–823.

[8] J.A. Paradiso, T. Starner, Energy scavenging for mobile and wireless electronics, *IEEE Pervasive Computing* 4 (2005) 18–27.

[9] H. Sodano, D.J. Inman, G. Park, A review of power harvesting from vibration using piezoelectric materials, *Shock and Vibration Digest* 36 (2004) 197–205.

[10] H. Sodano, D.J. Inman, G. Park, Generation and storage of electricity from power harvesting devices, *Journal of Intelligent Material Systems and Structures* 16 (2005) 67–75.

[11] S. Roundy, On the effectiveness of vibration-based energy harvesting, *Journal of Intelligent Materials and Structures* 16 (2005) 809–823.

[12] N. duToit, B. Wardle, Experimental verification of models for microfabricated piezoelectric energy harvesters, *AIAA Journal* 45 (2007) 1126–1137.

[13] A. Erturk, D. Inman, A distributed parameter electromechanical model for cantilevered piezoelectric energy harvesters, *Journal of Vibration and Acoustics* 130 (2008) 041002.

[14] S. Roundy, Y. Zhang, Toward self-tuning adaptive vibration-based micro-generators, *Smart Materials, Nano- and Micro-Smart Systems*, Sydney, Australia, 2005, pp. 373–384.

[15] N.G. Stephen, On energy harvesting from ambient vibration, *Journal of Sound and Vibration* 293 (2006) 409–425.

[16] W. Wu, Y. Chen, B. Lee, J. He, Y. Peng, Tunable resonant frequency power harvesting devices, *Proceedings of Smart Structures and Materials Conference*, SPIE, San Diego, CA, 2006, p. 61690A.

[17] V. Challa, M. Prasad, Y. Shi, F. Fisher, A vibration energy harvesting device with bidirectional resonance frequency tunability, *Smart Materials and Structures* 75 (2008) 1–10.

[18] S.M. Shahruz, Design of mechanical band-pass filters for energy scavenging, *Journal of Sound and Vibrations* 292 (2006) 987–998.

[19] R. Masana, M.F. Daqaq, Electromechanical modeling and nonlinear analysis of axially-loaded energy harvesters, *Journal of Vibration and Acoustics* 133 (2011) 011007.
[20] E. Leland, P. Wright, Resonance tuning of piezoelectric vibration energy scavenging generators using compressive axial preload, *Smart Materials and Structures* 15 (2006) 1413–1420.
[21] D. Barton, S. Burrow, L. Clare, Energy harvesting from vibrations with a nonlinear oscillator, *Proceedings of the ASME 2009 International Design Engineering Technical Conference and Computers and Information in Engineering Conference*, San Diego, CA, 2009.
[22] D. Quinn, D. Vakakis, L. Bergman, Vibration energy harvesting with essential nonlinearities, *Proceedings of the ASME 2007 International Design Engineering Technical Conference and Computers and Information in Engineering Conference*, Las Vegas, NV, 2007.
[23] F. Cottone, H. Vocca, L. Gammaitoni, Nonlinear energy harvesting, *Physical Review Letters* 102 (2009) 080601.
[24] B.P. Mann, B.A. Owens, Investigations of a nonlinear energy harvester with a bistable potential well, *Journal of Sound and Vibration* 329 (2010) 1215–1226.
[25] S.C. Stanton, C.C. McGehee, B.P. Mann, Nonlinear dynamics for broadband energy harvesting: investigation of a bistable piezoelectric inertial generator, *Physica D: Nonlinear Phenomena* 239 (2010) 640–653.
[26] A. Erturk, J. Hoffman, D.J. Inman, A piezo-magneto-elastic structure for broadband vibration energy harvesting, *Applied Physics Letters* 94 (2009) 254102.
[27] S. Stanton, C.C. McGehee, B. Mann, Reversible hysteresis for broadband magnetopiezoelastic energy harvesting, *Applied Physics Letters* 95 (2009) 174103.
[28] M.F. Daqaq, Response of uni-modal duffing type harvesters to random forced excitations, *Journal of Sound and Vibration* 329 (2010) 3621–3631.
[29] D. Barton, S. Burrow, L. Clare, Energy harvesting from vibrations with a nonlinear oscillator, *Journal of Vibration and Acoustics* 132 (2010) 021009.
[30] C. McInnes, D. Gorman, M. Cartmell, Enhanced vibrational energy harvesting using nonlinear stochastic resonance, *Journal of Sound and Vibration* 318 (2008) 655–662.
[31] L.N. Virgin, *Vibration of Axially-Loaded Structures*, Cambridge University Press, NY, 2007.